Theory-Guided Defect Tuning through Topochemical Reactions for Accelerated Discovery of UVC Persistent Phosphors

Hong Li, Qi Liu, Ju-Ping Ma, Zhao-Yang Feng, Jian-Dang Liu, Qing Zhao, Yoshihiro Kuroiwa, Chikako Moriyoshi, Bang-Jiao Ye, Jun-Ying Zhang, Chang-Kui Duan,* and Hong-Tao Sun*

Long persistent phosphors (LPPs) have attracted enduring attention owing to their wide applications. However, the discovery of LPPs is thus far largely the results of trial and error. Here, theory-guided defect tuning through topochemical reactions is demonstrated for accelerated discovery of emerging LPPs. First-principles calculations are employed to identify the thermodynamic charge-transition levels of different defect states, which help examine whether the candidate structure is a suitable host for afterglow. Rationally tuning the species and concentrations of defects through topochemical reactions is then illustrated, which leads to discovery of Pr^{3+}-doped $LaPO_4$ featuring ultraviolet C afterglow with a lasting time of over 2 h. Such a strategy, in conjunction with advanced characterizations including high-resolution synchrotron X-ray diffraction, positron annihilation lifetime spectroscopy, and electron spin resonance, suggests a radical-involved afterglow mechanism. Importantly, it is illustrated that this concept can be extended for the discovery of more LPPs. It is suggested that theory-guided defect engineering enabled by topochemical reactions can be used as a powerful tool to accelerate discovery of novel LPPs with much clearer afterglow mechanisms, with implications even for the design of other optoelectronic materials.

1. Introduction

Long persistent phosphors (LPPs) have garnered enduring interest of materials scientists, chemists, physicists, and even biologists owing to their long-lived phosphorescence and the

widespread applications.[1–16] The biggest difference between LPPs and fluorescent materials is that the former can store the excitation energy in excited states and then slowly release it as light. This delayed light emission, commonly referred to as long persistent luminescence or afterglow, arises from the thermally activated detrapping of trapped charge carriers that are created by light excitation and subsequent trapping at certain defect sites.[1,15] Until now, LPPs emitting in the visible, near-infrared, and ultraviolet spectral regions, with afterglow duration of several hours or even several hundreds of hours, have been developed.[1,5,11,17] However, in most cases the creation and tuning of defect-correlated charge-carrier trapping centers have thus far largely been the results of trial and error.[1,18,19] Furthermore, in surprisingly few cases does one have a detailed understanding of the underlying defect structure and the corresponding charge carrier trapping–detrapping process. As a consequence, tuning of structural defects that contribute to the charge-carrier trapping in a rational manner could not only provide new chances to accelerate discovery of LPPs, but also gain deep insights into the mechanism of long persistent luminescence.

Computational methods have been identified as a powerful tool to guide materials synthesis either by predicting structures

H. Li, Q. Liu, J.-P. Ma, Prof. H.-T. Sun
College of Chemistry
Chemical Engineering and Materials Science
Soochow University
Suzhou 215123, P. R. China
E-mail: timothyhsun@gmail.com
Z.-Y. Feng, Prof. C.-K. Duan
Department of Physics
University of Science and Technology of China
Hefei 230026, P. R. China
E-mail: ckduan@ustc.edu.cn

The ORCID identification number(s) for the author(s) of this article can be found under https://doi.org/10.1002/adom.201901727.

DOI: 10.1002/adom.201901727

Dr. J.-D. Liu, Prof. B.-J. Ye
State Key Laboratory of Particle Detection and Electronics
Department of Modern Physics
University of Science and Technology of China
Hefei 230026, P. R. China
Q. Zhao, Prof. Y. Kuroiwa, Prof. C. Moriyoshi
Department of Physical Science
Hiroshima University
Hiroshima 739-8526, Japan
Prof. J.-Y. Zhang
Key Laboratory of Micro-Nano Measurement
Manipulation and Physics (Ministry of Education)
School of Physics
Beihang University
Beijing 100191, P. R. China

with specific compositions or by assessing the electronic features and other properties of some targeted systems before experiment, with notable successes.[20,21] This has led to accelerated synthetic discovery of new functional materials with desirable physiochemical properties. Nevertheless, to the best of our knowledge, employing computational methods to rationally tuning structural defects has not received deserved attention in previous works.[1] Given that LPPs rely on the trapping of excited carriers by structural defects, we therefore took the view that theory-guided defect tuning could facilitate screening of candidate structures with optimized defect species and amount that favor afterglow, which is of particular importance for searches for emerging ultraviolet C (UVC) LPPs because of their present-day scarce types and huge potential in terms of sterilization, disinfection, cancer therapy, and so on.[11,12] We also held a point of view that, through theory-driven intentional manipulation of defect states, we could gain a robust understanding of the underlying afterglow mechanism, which would in turn further promote more rational design of LPPs.

Considering that structural defects play a particularly important role in governing the trapping of excited charge carriers and then the afterglow properties, we reasoned that exploring facile chemical routes to defect tuning could offer an efficient way to rationally control and optimize the afterglow properties. Recently, low-temperature topochemical reactions, involving mild deintercalation of constituent atoms while conserving the original structural features have emerged as a powerful technique to create a large number of metastable phases with unconventional electronic, magnetic, catalytic, and optical properties.[22–29] Nevertheless, the employment of topochemical reactions for the control and optimization of the properties of LPPs have never been explored. Since this "soft" chemical route can give rise to different defects in a targeted system, such as atomic vacancies and vacancy complexes, we thus hypothesized that it could be used for the creation of structural defects that function as charge-carrier traps.

Herein, we report the use of theory-guided defect tuning experimentally enabled by topochemical reactions for accelerated discovery of emerging LPPs. We first examine the formation energies and the corresponding charge-transition levels of various point defects and defect complexes in an orthophosphate model system through systematic first-principles density functional theory (DFT) calculations, which indicate that introducing vacancy pairs and more complex defects facilitates the creation of shallow trap states with respect to the conduction and valence bands. We then show that such defects can be incorporated into the as-synthesized product through a solid-state reaction, which renders UVC afterglow occur because of slow release of trapped charge carriers via the $4f5d$-$4f^2$ transition of doped Pr^{3+} ions. Importantly, we demonstrate that a postsynthetically topochemical reaction can be used for creation and conversion of different defects governing the charge trapping–detrapping process, which enables stronger UVC afterglow. Based on structural characterizations including high-resolution synchrotron X-ray diffraction (XRD), positron annihilation lifetime spectroscopy (PALS), and electron spin resonance (ESR), we discover that the charge trapping and detrapping processes are intimately associated with the dynamic changes in phosphorus–oxygen radicals, which leads

us to propose a radical-involved afterglow mechanism. We finally demonstrate that our finding can trigger the discovery of other LPPs operating in the UVC and even other spectral range.

2. Results and Discussion

We chose lanthanum orthophosphate as a model system for our study (Figure S1, Supporting Information), with the idea that it can exhibit various structural defects such as atomic point defects, defect complexes, and radicals, and possess large band gaps that is suitable for UVC afterglow.[30–36] We began by carrying out first-principles DFT calculations aimed at probing whether such defects hold potential to function as traps required for afterglow. The calculated bandgap of monoclinic $LaPO_4$ is 5.19 eV (Figure S2, Supporting Information), relatively smaller than the experimental value of 6.40 eV.[34] The formation energies of oxygen vacancies with different charges suggest that O3 vacancies with +2 (V_{O3}^{2+}) preferentially form in the structure (Table S1, Supporting Information). We also calculated the formation energies of oxygen-vacancy pairs with different charges, indicating that $V_{O3,1}^{2+}$ (vacancy pair of one O3 and one O1 vacancy formed in one $[PO_4]$ unit) has the lowest formation energy (Table S2, Supporting Information).

To examine the trap depths with respect to the conduction and valence bands, we next calculated the thermodynamic charge-transition levels of different defect states. As displayed in **Figure 1** and Figures S3–S14 (Supporting Information), we find that all charge-transition levels of oxygen vacancies situate at >0.5 eV above the maximum of the valence band, which could act as hole trapping centers, in particular for the $\varepsilon(+2/+1)$ level of V_{O4}. In marked contrast, oxygen vacancy pairs can introduce shallow trap levels near the conduction band, accompanied by deep ones. For instance, the $\varepsilon(-1/-2)$ level of $V_{O3,1}$, the $\varepsilon(0/-1)$ level of $V_{O3,3}$ (simultaneous formation of O3 vacancy in nearby two $[PO_4]$ units), and the $\varepsilon(0/-2)$ level of $V_{O3,4}$ are <0.25 eV below the minimum of the conduction band. We note that $V_{O3,3}$ can introduce trap levels near the conduction and valence bands. We also considered the possible cationic vacancies, based on the fact that the phosphorus source is easily evaporated during the synthesis. Interestingly, we reveal that, introducing V_P, V_{PO3} (simultaneous formation of one P and
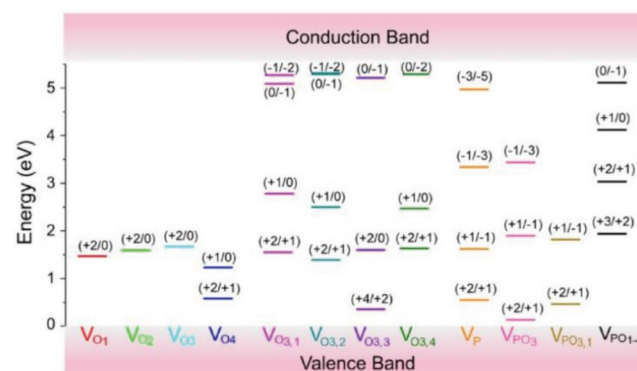

Figure 1. Calculated thermodynamic charge transition levels for native defects in $LaPO_4$. O1, O2, O3, and O4 atoms coordinate with P in one $[PO_4]$ tetrahedron.

one O3 vacancy in one [PO$_4$] unit), $V_{PO3,1}$, and V_{PO1-4} (one P and four O vacancies in one [PO$_4$] unit) causes the occurrence of a series of shallow trap levels near the conduction and/or valence bands. We point out that the suitable trap depth for room temperature afterglow is around 0.6 eV with respect to the conduction or valence band.[1,37] Although the DFT method used here underestimate the bandgap, the presence of a series of charge-transition levels of different defect states leads us to hypothesize that these defects in LaPO$_4$ could act as trap centers for afterglow.

To test this hypothesis, we synthesized Pr^{3+}-doped LaPO$_4$ with a nominal composition of La$_{(1-x)}$PO$_4$:xPr^{3+} by a solid-state reaction method. The reason for using Pr^{3+} as a dopant lies in its capability of UVC emissions corresponding to the 4f5d-4f^2 transition.[38–40] In the monoclinic LaPO$_4$ crystal, La and P atoms coordinate with nine and four O atoms, respectively (Figure S1, Supporting Information). Laboratory XRD shows that incorporating Pr^{3+} ions does not introduce any new phase different from LaPO$_4$ (Figure S15, Supporting Information). We then conducted the high-resolution synchrotron XRD measurement at room temperature for the typical sample, La$_{0.9925}$PO$_4$:0.0075Pr^{3+}, to gain more structural information of Pr^{3+}-doped LaPO$_4$. Rietveld refinement of the synchrotron XRD data has been conducted using the general structure analysis system (GSAS) software package.[41] We first refined the background, cell parameters, pseudo-Voigt peak profile coefficients, atomic coordinates, and isotropic displacement factors for all atoms. After that, we refined the occupancies of phosphorus and oxygen atoms. We note that the refinement adequately converged to $R_{wp} = 4.93\%$ and $R_p = 3.74\%$, with reasonable isotropic displacement factors for all atoms, yielding a chemical composition of La(Pr)P$_{0.974}$O$_{3.607}$ (**Figure 2**a; Table S3, Supporting Information). This strongly signifies the existence of a high density of oxygen and phosphorus vacancies in the lattice. Different from very small amounts of atomic vacancies in some products synthesized by solid-state reactions, the emergence of a considerable density of atomic vacancies in our case can be accounted for by a solid-state topochemical reaction occurring at high temperatures, possibly as a consequence of the low defect formation energy and the ready evaporation of phosphorus source.

We then proceeded to examine whether the as-synthesized defective Pr^{3+}-doped LaPO$_4$ shows UVC afterglow. Considering the large bandgap of LaPO$_4$, we chose X-ray as the excitation source to efficiently charge the phosphors. Interestingly, as expected, after X-ray irradiation the phosphors exhibit UVC afterglow emission with an emission maxima at 231 nm originating from the 4f5d→^{3}H$_4$ transition of Pr^{3+} ions, accompanied by relatively weak UVA and visible afterglow assigned to the host and the 4f^2-4f^2 intraconfigurational transitions, respectively (Figure 2b; Figure S16, Supporting Information).[38] We emphasize that the

afterglow duration and intensity depend on the doping concentrations of Pr^{3+} and X-ray irradiation time (Figures S17 and S18, Supporting Information). Figure 2c shows images of the UVC afterglow at room temperature, recorded using a UVC imager. Remarkably, the afterglow intensity decreases quickly in the first few minutes and then slowly decreases. We find that heating the 24 h decayed product at 200 °C leads to UVC emissions that last for 30 s, and that irradiating it using a 450 nm laser also causes such emissions with a lasting time over 100 s (Figure S19, Supporting Information). These observations unambiguously indicate that our as-prepared, defective Pr^{3+}-doped LaPO$_4$ can show afterglow and also suggest that, besides shallow traps suitable for room temperature afterglow, some charge carriers are trapped in deep traps. We underscore that the afterglow monitored at 231 nm for the best sample, La$_{0.9925}$P$_{0.974}$O$_{3.607}$:0.0075Pr^{3+} (abbreviated as LPPO hereafter), lasts over 2 h after X-ray irradiation for 600 s that corresponds to a dose of 12 Gy (**Figure 3**a). We note that under the excitation of 200 nm UV light for 5 min, we did not observe any afterglow, which can be ascribed to the large bandgap of LaPO$_4$ that makes charging impossible.

Aiming at optimizing the afterglow properties, we next sought to tune the defect states in Pr^{3+}-doped LaPO$_4$ through a postsynthetically topochemical reaction using CaH$_2$ as oxygen getters (see details in the Experimental Section). The key is to extract oxygen atoms in the lattice for intentional creation of a higher concentration of shallow traps that can favor stronger room-temperature UVC afterglow. The samples were denoted Ca–T–t, where T and t represent the treatment temperature in degree centigrade and the duration in hours, respectively. We note that such a mild treatment cannot affect the crystalline
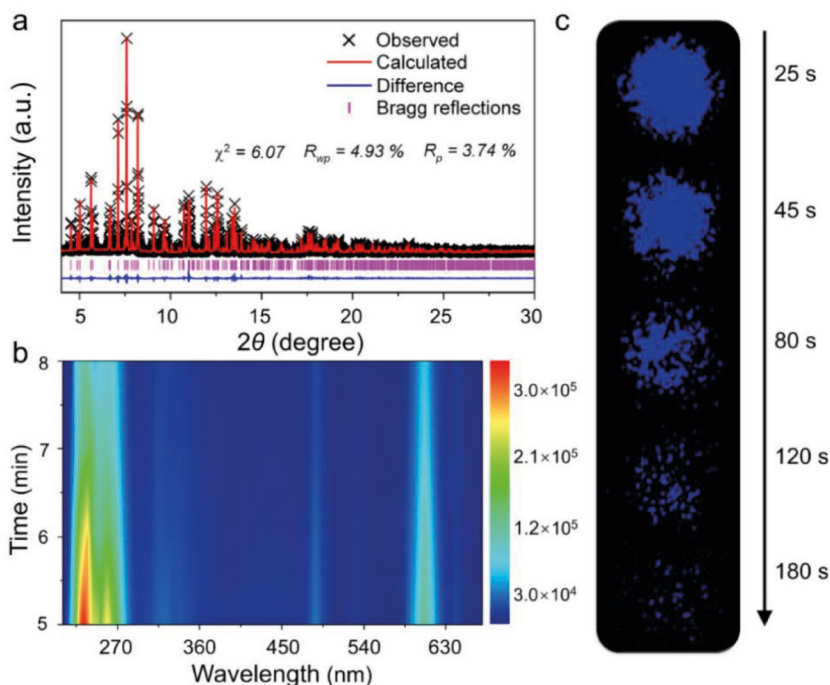

Figure 2. a) Rietveld fit to the high-resolution SXRD pattern. b) Time-dependent afterglow spectra and c) UVC images of the as-synthesized LPPO taken at different times after ceasing X-ray irradiation.
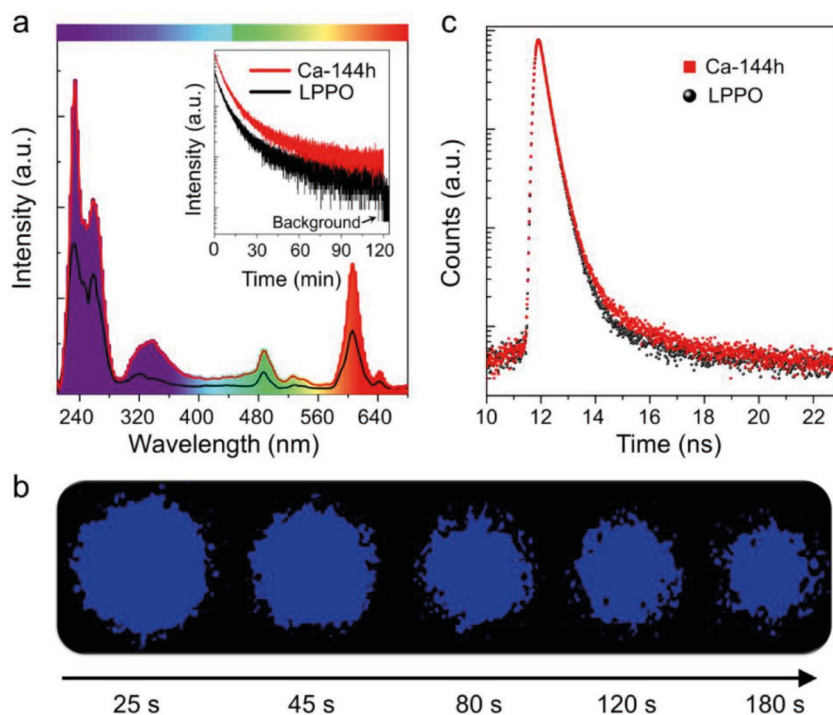
ADVANCED
SCIENCE NEWS
www.advancedsciencenews.com

ADVANCED
OPTICAL
MATERIALS
www.advopticalmat.de

Figure 3. a) Afterglow spectra of the as-synthesized LPPO and Ca-144h sample recorded at 5 min after stopping X-ray irradiation. Inset: UVC afterglow curves monitored at 231 nm. b) UVC images of the Ca-144h sample taken at different times after ceasing X-ray irradiation and c) positron lifetime spectra of the as-synthesized LPPO and Ca-144h sample.

phase and the morphology of the sample (Figures S20 and S21, Supporting Information). The photoluminescence of the reduced phosphors exhibits decreased intensity with the increase of treatment time (Figure S22, Supporting Information). We find that the afterglow behaviors are closely associated with the treatment temperature and duration; the optimal temperature is confirmed to be 500 °C (Figure S23, Supporting Information), and 144 h of treatment duration produces the strongest UVC afterglow (Figure S24, Supporting Information). Surprisingly, the initial UVC afterglow intensity of the best reduced phosphor is 1.4 times stronger than that of the as-synthesized one, with an afterglow over 2 h after ceasing X-ray irradiation (Figure 3a,b). Additionally, thermally- and light-stimulated UVC emissions, combined with the thermoluminescence measurements, indicate that a higher concentration of deep traps exist in the reduced sample compared with the as-synthesized one (Figures S19 and S25–S27, Supporting Information). We underscore that, although topochemical reactions have been employed for tuning the properties of some luminescent materials,[27,28] for the first time it is used for the optimization of the properties of LPPs.

It is well recognized that knowing the species of defects is prerequisite for a robust understanding of the afterglow mechanism. We therefore took the PALS measurement of the as-synthesized and the best reduced samples, considering that it can provide crucial information regarding the species and relative concentrations of structural defects, even at a parts-per-million level.[42,43] The positron lifetime spectra of both samples exhibit three fitted lifetime components (Figure 3c, **Table 1**).

The longest component (τ_3) can be tentatively attributed to large voids such as vacancy clusters.[43] Based on the calculated positron lifetimes (**Table 2**), the shortest lifetime component (τ_1) can be ascribed to the positron trapped at oxygen divacancies ($V_{O3,1}$, $V_{O3,2}$, and $V_{O3,4}$; a class of defects due to the loss of two oxygen atoms from the [PO_4] unit), while the component (τ_2) can be assigned to vacancy associates (V_{PO1-4}) (**Figure 4**). We point out that the relative intensity (i.e., I_1, I_2, and I_3) of positron lifetimes can quantify the abundance of these defects, which indicate that oxygen divacancies are predominant in both samples, accompanied by relatively less vacancy associates (V_{PO1-4}) and large voids (Table 1).

In light of all these observations, it is reasonable to link the enhanced room-temperature UVC afterglow and stronger thermally- and light-stimulated emissions in the reduced sample to the increased concentrations of oxygen divacancies and large voids, respectively. We then focus on the elucidation of the UVC afterglow mechanism through examining the charge carrier trapping–detrapping process in the best reduced sample. Considering that this process is closely related to the change in the charge-carrier state, we thus tried to monitor it by ESR. Note that here we mainly discuss the defects closely associated with the room-temperature UVC afterglow. The formation of oxygen vacancies, either in the synthesis or the postsynthetically topochemical treatment, can be described by the following equation, where the Kröger–Vink notation is used

$$O \rightarrow \frac{1}{2}O_2 + V_O^{\bullet\bullet} + 2e^- \tag{1}$$

Simultaneous formation of two oxygen vacancies in one [PO_4] tetrahedron can result in the occurrence of undercoordinated P–O unit, namely, [PO_2]. As shown in **Figure 5**a, before X-ray irradiation the sample shows an ESR signal with $g = 2.0002$ and a line width of 34 G, which can be assigned to the [PO_2]$^{\bullet 2-}$ radical that also exists in other phosphorus-containing compounds.[35] The presence of the [PO_2]$^{\bullet 2-}$ radicals, due to the removal of two coordinated oxygen atoms from the [PO_4] structural units, is in consistence with the PALS result. Under X-ray irradiation, constituent atoms in the product interact with X-ray photons, and high-energy electrons are ejected from lattice atoms, accompanied by the creation of holes (process ① in Figure 5b); such ejected high-energy electrons produce secondary

Table 1. Positron lifetime parameters of LPPO and Ca-144h.

Sample	τ_1 [ps]	τ_2 [ps]	τ_3 [ps]	I_1 [%]	I_2 [%]	I_3 [%]
LPPO	210	372	2084	68.4	30.4	1.2
Ca-144h	217	404	2297	69.6	28.6	1.8

**ADVANCED
SCIENCE NEWS**
www.advancedsciencenews.com

**ADVANCED
OPTICAL
MATERIALS**
www.advopticalmat.de

Table 2. Calculated positron lifetimes of $LaPO_4$.

Defect	Bulk	$V_{O3,1}$	$V_{O3,2}$	$V_{O3,4}$	V_{PO1-4}
Lifetime [ps]	186.5	192.4	190.0	192.1	326.6

high-energy electrons. These created hot charge carriers are then subject to thermalization and captured by traps in the lattice (process ② and ③). Interestingly, the X-ray-irradiated sample shows one ESR signal with $g = 2.0058$ and a line width of 50 G, which is wider and stronger than that without irradiation (Figure 5a; Figure S28, Supporting Information). This signal can be assigned to the $[PO_2]^{•0}$ radical that can form as follows[44]

$$[PO_2]^{•2-} \rightarrow [PO_2]^{•0} + 2e^- \tag{2}$$

Furthermore, the stronger intensity of the $[PO_2]^{•0}$ radical suggests that other processes may also involve its formation. We surmise that the some ESR-inactive phosphorus–oxygen units, such as the $[PO_2]^-$ unit, can be transformed into the $[PO_2]^{•0}$ radical under X-ray irradiation, which can be shown by the following equation

$$[PO_2]^- \rightarrow [PO_2]^{•0} + e^- \tag{3}$$

Besides, two weak peaks at $g = 2.0682$ and 2.0648 in the irradiated sample can be attributed to the $O^{•-}$ radical.[45] Subsequently, the released excited electron can be captured by oxygen divacancies

$$2V_O^{••} + 2e^- \rightarrow 2V_O^{•} \tag{4}$$

where $2V_O$ denotes oxygen divacancies. After undergoing the processes (①–③), the energy storage can be realized. We note that the charge-transition levels of oxygen divacancies are near the conduction band (Figure 1), which allows the trapped electrons thermally detrap into the conduction band at room temperature (process ④). We surmise that the holes probably couple with the Pr^{3+} ions (process ⑤), and when the detrapped electrons are down to the 5d band of the Pr^{3+}, we can view the formation of excited Pr^{3+} ions, which subsequently gives rise to the UVC afterglow (process ⑥). After 24 h decay,

the sample shows nearly identical ESR with that before X-ray irradiation; this nearly synchronous changes in the ESR and afterglow, combined with the exact identification of defect species in our system (Figure 3c and Tables 1 and 2), suggest that the phosphorus–oxygen radicals involve in the afterglow. The charge-carrier release and recapture by the phosphorus–oxygen radicals can be described based on the following equations

$$2V_O^{•} \rightarrow 2V_O^{••} + 2e^- \tag{5}$$

$$[PO_2]^{•0} + 2e^- \rightarrow [PO_2]^{•2-} \tag{6}$$

That is, the stored energy is released in the form of photons through electron migration and recombination with holes, in which Pr^{3+} ions act as the energy release channel. We point out that the exact coupling between traps and Pr^{3+} ions still remains unclear, although our results unambiguously signify that the phosphorus–oxygen radicals involve in the afterglow.

We underscore that the ESR results suggest that the sample can be repeatedly charged by X-ray, which is in an excellent agreement with our experimental result (Figure S29, Supporting Information). Collectively, the room-temperature afterglow shown in our product can be considered to be dominated by a radical-involved electron trapping and detrapping process. We emphasize that deep traps as shown in Figure 1 also involve the trapping of charge carriers, as suggested by the thermoluminescence and photostimulated luminescence measurements (Figures S19 and S25–S27, Supporting Information). Although the afterglow intensity of the best sample reported here is weaker than that of previously reported Pr^{3+}-doped Cs_2NaYF_6 (Figure S30, Supporting Information),[11] our work clearly shows that intentional creation of defects favoring afterglow in targeted systems can be adopted as a powerful tool for rational design of persistent phosphors with much clearer afterglow mechanisms. We note that the defective $LaPO_4$ can be used as a host not only for UVC afterglow, but also for afterglow in other spectral range. For instance, by using Tb^{3+} ions as emitters, the as-synthesized product demonstrates UVA afterglow with a duration of more than 2 h (Figure S31, Supporting Information). Additionally, we further find that other compounds with phosphorus–oxygen groups such as pyrophosphates can also be employed as hosts for UV afterglow (Figure S32, Supporting
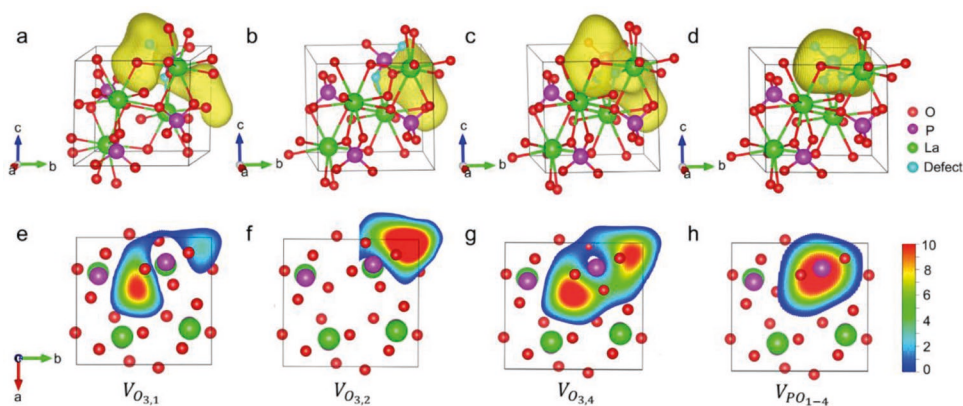

Figure 4. a–d) Positron density distribution (yellow) in $LaP_{1-x}O_{4-y}$ with a) $V_{O3,1}$, b) $V_{O3,2}$, c) $V_{O3,4}$, and d) V_{PO1-4} defects. e–h) Positron density in $LaP_{1-x}O_{4-y}$ along the (001) plane for the trapped positrons of e) $V_{O3,1}$, f) $V_{O3,2}$, g) $V_{O3,4}$, and h) V_{PO1-4} defects.

**ADVANCED
SCIENCE NEWS**
www.advancedsciencenews.com

**ADVANCED
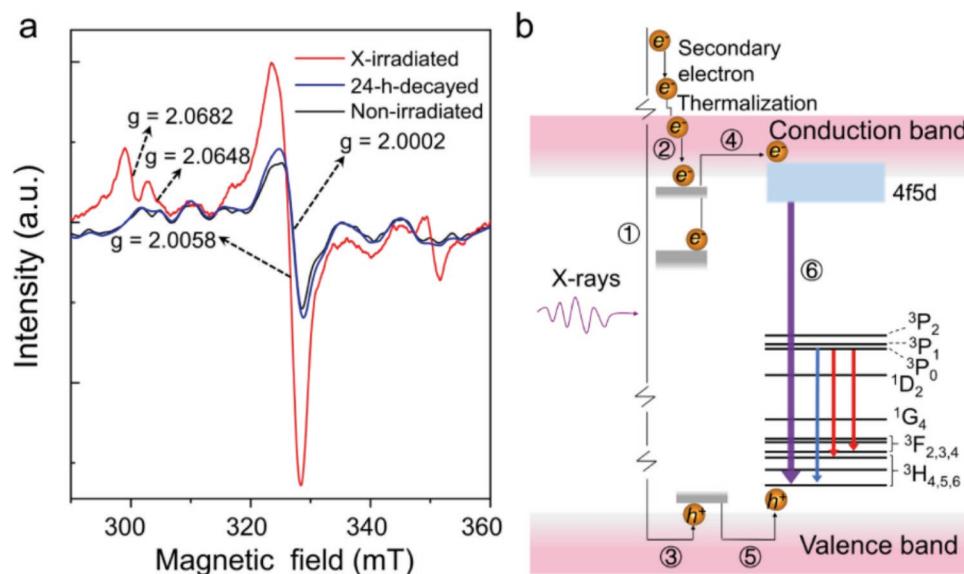OPTICAL
MATERIALS**
www.advopticalmat.de

Figure 5. a) ESR spectra of the Ca-144h sample before and after X-ray irradiation, and 24 h decay. b) Schematic illustration of the proposed afterglow mechanism. The solid black arrows represent electronic transitions. The gray rectangles denote electron and hole trap states. Oxygen divacancies and large voids act as the shallow and deep electron traps, respectively. The purple, blue, and red arrows represent the optical transitions corresponding to the UVC, blue, and red emissions, respectively.

Information), which probably is dominated by a similar afterglow mechanism deserving to be further studied.

3. Conclusion

To summarize, we have demonstrated that theory-guided defect tuning through topochemical reactions, superior to the traditional method of trial and error, can be used for rational design of emerging LPPs, thus accelerating their discovery. First-principles calculations enabled us to identify that defective $LaPO_4$ could be employed as a candidate host for afterglow, considering the different defect states. The exact defects are subsequently identified experimentally, suggesting the dominant presence of the $[PO_2]$ defects. We demonstrated that the species and concentrations of structural defects in Pr^{3+}-doped $LaPO_4$ can be rationally tuned through topochemical reactions, which leads us to create one class of UVC LPPs with a lasting time as long as 2 h. Importantly, we showed that such a theory-guided defect tuning, combined with a wide range of advanced characterizations including the synchrotron XRD, PALS, and ESR, can lead us to gain a robust understanding of the radical-involved afterglow mechanism. We finally demonstrated that our finding can be extended for the design and discovery of more emerging LPPs. We envisage that our work opens up possibilities of accelerating discovery of novel LPPs and even other optoelectronic materials.

4. Experimental Section

Synthesis of Persistent Phosphors: Pr^{3+} doped $LaPO_4$ with the nominal composition of $La_{(1-x)}PO_4:xPr^{3+}$ (x = 0.0025, 0.0050, 0.0075, 0.010, and 0.030) was synthesized using a traditional high-temperature solid-state

reaction method. The chemicals, La_2O_3 (Alfa Aesar, 99.999%), $NH_4H_2PO_4$ (3 mol% excess, Aladdin, 99.99%), and Pr_6O_{11} (Alfa Aesar, 99.996%) were used as received. Stoichiometric amounts of La_2O_3, $NH_4H_2PO_4$, and Pr_6O_{11} were homogeneously mixed and ground and then first sintered in alumina crucible at 500 °C for 4 h in air. The resulting powders were then reground, and finally sintered at 1350 °C in air for 4 h. After cooling to room temperature naturally, the as-obtained white powder collected and stored for further characterization. Alumina crucible with a purity of 99% was used as vessels in the above experiment.

Topochemical Treatment of As-Synthesized Persistent Phosphors: The as-synthesized $La_{0.9925}PO_4:0.0075Pr^{3+}$ was topochemically treated by using CaH_2 (dry, Aladdin, 98.5%) as an oxygen getter in a sealed glass tube under vacuum. CaH_2 was not mixed with the material to avoid contamination. Approximately 0.17 g of powder was placed in a small semiclosed glass tube and then this was placed in a larger and longer glass tube with four mole equivalent of CaH_2 powder. All operations were performed in a nitrogen-filled glovebox (O_2 and H_2O < 0.1 ppm). The larger tube was then flame sealed under vacuum. The tubes were then heated at temperatures ranging from 200 to 560 °C for different durations.

Structural and Morphological Characterization: Laboratory XRD patterns were recorded at room temperature with a Bruker D2 PHASER diffractometer with Cu Kα radiation source (λ = 1.5418 Å). High-resolution synchrotron XRD experiments for the structural refinement were performed on SPring-8 BL02B2 of the Japan Synchrotron Radiation Research Institute (JASRI) to obtain high-quality diffraction patterns at room temperature. The fine powder sample for high-resolution synchrotron XRD was sealed into Hilgenberg glass capillary with an internal diameter of 0.1 mm. The capillary was rotated during the measurement to reduce the preferred orientation effect and to average the intensity. The X-ray wavelength used is 0.41410 Å. Rietveld structural refinement was preformed against the XRD data utilizing the GSAS program. Field-emission scanning electron microscopy images were obtained by using a Hitachi SU8010 scanning electron microscope operating at 10 kV accelerating voltage. Low-temperature ESR spectra were performed on an ESR spectrometer (JEOL JES-X320) at 173 K.

Photoluminescence, Afterglow, and Thermoluminescence Characterizations: Downconversion luminescence spectra were

1901727 (6 of 8)

**ADVANCED
SCIENCE NEWS**

www.advancedsciencenews.com

**ADVANCED
OPTICAL
MATERIALS**

www.advopticalmat.de

recorded with a monochromator (iHR550, Horiba) equipped with a PMT (Hamamatsu, R928) under the excitation of a 450 nm laser diode. Upconversion luminescence spectra were recorded with a monochromator (iHR550, Horiba) equipped with a PMT (Hamamatsu, R928) under the excitation of a 450 nm laser diode. The excitation power density is 8.78 W cm^{-2}. Persistent luminescence spectra and persistent decay curves were measured using an FLS980 fluorescence spectrophotometer (Edinburgh Instruments Ltd.) equipped with a photomultiplier (R928P with an applied voltage of 950 V, Hamamatsu) at different duration after stoppage of X-ray irradiation. 0.02 g powders in aluminum plates (one powder in one plate) were irradiated with the above X-ray irradiator for 600 s that corresponds to a dose of 12 Gy, after stoppage the irradiation for 5 min, the persistent spectra and decay curves were recorded with EM slit of 10 nm. The time schedule for each measurement was the same. Thermoluminescence glow curves were measured with an FJ-427A1 thermoluminescent dosimeter, with a heating rate of 1 °C s^{-1} from 35 to 350 °C. 0.2 g powder was first irradiated with an RS-2000 biological irradiator equipped with a tungsten target (160 kV, 25 mA) for 600 s at room temperature, and then were left for 48 h before the thermoluminescence measurement.

Real-Time Afterglow Measurements by a UVC Imager: UVC images were recorded by a homemade visible-blind UVC imager. The UVC signals from the samples, which were recorded as the number of photons in the corresponding UVC imager. The area of blue regions in the UVC images corresponds to the intensity of UVC afterglow; the larger the area, the stronger the afterglow. To avoid photon count saturates, a relatively low applied voltage (1.80 V) was used in the process of recording initial UVC images. The initial UVC images were taken in different time intervals after stopping the X-ray irradiation. The distance between the imager and the sample was 100 cm. Photostimulated UVC images of the 24 h decayed phosphors were recorded from 1 s after turning on the laser irradiation of 450 nm with a power density of 1.27 W cm^{-2}. Thermostimulated UVC images of the 24 h decayed phosphors were taken from 4 s after putting the sample on the hot plate; the temperature of the hot plate is 200 °C. Both photostimulated and thermostimulated UVC images were taken at 24 h after stoppage of X-ray irradiation.

Positron Annihilation Measurement: To conduct the positron lifetime experiments, the as-prepared samples were pressed into round disc with diameter of 8 mm and thickness of 1 mm, and then a 20 µCi positron source of ^{22}Na was sandwiched between two identical samples. The positron lifetime experiments were carried out with an ORTEC fast-fast coincidence system with a time resolution of about 200 ps in full width at half maximum at room temperature, and the total counts of each lifetime spectrum exceeded three million. Positron lifetime spectra were deconvoluted by using the LT9 code. One channel represented the time of 12.7 ps. Positron lifetime calculations were performed using the ATSUP method and the generalized gradient approximation, in which the electron density and the positron crystalline Coulomb potential were constructed by the non-self-consistent superposition of free atom electron density and Coulomb potential in the absence of the positron. The model of $2 \times 2 \times 2$ supercells was used for positron lifetime calculations of LaPO$_4$ with unrelaxed structure vacancy. The crystal structure and electron-density distribution were drawn with the program VESTA.

Geometric Optimizations and Band Structural Calculations: The initial atomic positions and symmetry information of the host crystal were taken from the Inorganic Crystal Structure Database. GGA-PBEsol calculations were adopted for atomic relaxation, as implemented in the Vienna ab initio simulation package (VASP).[46–50] The La (5s^{2}5p^{6}6s^{2}5d^1), P (3s^{2}3p^3), and O (2s^{2}2p^4) were treated as valence electrons, and their interactions with the cores were described by the projector augmented wave method.[51] Band structure calculations of the host material LaPO$_4$ were carried out in VASP by utilizing fully self-consistent calculations with 75 k-points centered at Γ point following the Automatic-mesh scheme,[52] and then 113 k-points containing ['Z', 'G', 'Y', 'A', 'B', 'D', 'E', 'C'] were set to perform a non-self-consistent calculation to complete the band structure calculations. Plane-wave cut-off energies were set at 400 eV following the previous paper.[53] The defects of various oxygen

vacancies, P vacancies and clustering of those vacancies were modeled by removing appropriate atoms from a $1 \times 2 \times 2$ supercell containing 96 atoms. The structural relaxation was performed by utilizing the conjugate gradient technique. The equilibrium structures were obtained by optimizing atomic positions until the energy change was less than 10^{-6} eV and the Hellmann–Feynman forces on atoms were less than 0.01 eV Å^{-1}. The plane-wave cut-off energy was set to 400 eV and only one k-point Γ was used for sampling the Brillouin zone.

Formation Energy of Defects: The formation energy of defects V_P and V_O are calculated by using the expression

$$\Delta E_f\left[X^q\right] = \left(E_{tot}\left[X^q\right] + E_{corr}\right) - E_{tot}[bulk] - \sum_i n_i \mu_i + q(E_F + E_{VBM}) \tag{7}$$

where E_{tot} is the total energy of the optimized LaPO$_4$ supercell containing P vacancies and O vacancies, and E_{tot}[bulk] is the calculated total energies of perfect supercell. n_i are the numbers of the atoms of elements i, which are added to ($n_i > 0$) or removed from ($n_i < 0$) the perfect supercell. The analog of the chemical potential for "charge" is given by the chemical potential of the electrons, i.e., E_F is the Fermi level, referenced to the VBM of the bulk. As for the correction term E_{corr}, the primarily finite-size effects for charge defects were just included. μ_i is the atomic chemical potential of the element La, P, and O. Their atomic chemical potential are adopted

$$\mu_{La} = \frac{\mu_{La_2O_3} - 3\mu_O}{2} \tag{8}$$

$$\mu_P = \frac{\mu_{P_2O_5} - 5\mu_O}{2} \tag{9}$$

where La$_2$O$_3$ and P$_2$O$_5$ are the calculated total energy per formula unit for the La$_2$O$_3$ and P$_2$O$_5$, respectively. The chemical potential of O depends on the environment condition.

E_{corr} to account for electrostatic interactions between supercells,[54,55] i.e.,

$$E_{corr} = (1 + f)\frac{q^2 \alpha_M}{2\varepsilon L} \tag{10}$$

Here the meanings and values adopted in the calculations are: $1 + f \approx 2/3$, the net charge $q = +1$ for the LaPO$_4$ supercell with O vacancy in which one electron is removed so that a V_O^{1+} is created, the dielectric constant $\varepsilon \approx 3.658$, the linear supercell dimension $L = \Omega^{1/3} \approx 10.52$ Å (supercell volume Ω), and the Madelung-like constant $\alpha_M = 2.837$ for a cubic supercell.[56] Hence, E_{corr} is estimated to be about 0.35 eV for +1 charged O vacancy supercell.

Supporting Information

Supporting Information is available from the Wiley Online Library or from the author.

Acknowledgements

Conflict of Interest

The authors declare no conflict of interest.

Keywords

[1] Y. Li, M. Gecevicius, J. Qiu, *Chem. Soc. Rev.* **2016**, *45*, 2090.

[2] L. Gu, H. Shi, L. Bian, M. Gu, K. Ling, X. Wang, H. Ma, S. Cai, W. Ning, L. Fu, H. Wang, S. Wang, Y. Gao, W. Yao, F. Huo, Y. Tao, Z. An, X. Liu, W. Huang, *Nat. Photonics* **2019**, *13*, 406.

[3] Z. Gong, W. Zheng, Y. Gao, P. Huang, D. Tu, R. Li, J. Wei, W. Zhang, Y. Zhang, X. Chen, *Angew. Chem., Int. Ed.* **2019**, *58*, 6943.

[4] W. Li, W. Zhou, Z. Zhou, H. Zhang, X. Zhang, J. Zhuang, Y. Liu, B. Lei, C. Hu, *Angew. Chem., Int. Ed.* **2019**, *58*, 7278.

[5] T. Matsuzawa, Y. Aoki, N. Takeuchi, Y. Murayama, *J. Electrochem. Soc.* **1996**, *143*, 2670.

[6] X.-J. Wang, D. Jia, W. M. Yen, *J. Lumin.* **2003**, *102–103*, 34.

[7] D. Jia, L. A. Lewis, X.-J. Wang, *Electrochem. Solid-State Lett.* **2010**, *13*, J32.

[8] W. Yan, F. Liu, Y.-Y. Lu, X.-J. Wang, M. Yin, Z. Pan, *Opt. Express* **2010**, *18*, 20215.

[9] A. Abdukayum, J. T. Chen, Q. Zhao, X. P. Yan, *J. Am. Chem. Soc.* **2013**, *135*, 14125.

[10] Y. Li, Y. Li, R. Chen, K. Sharafudeen, S. Zhou, M. Gecevicius, H. Wang, G. Dong, Y. Wu, X. Qin, J. Qiu, *NPG Asia Mater.* **2015**, *7*, e180.

[11] Y. M. Yang, Z. Y. Li, J. Y. Zhang, Y. Lu, S. Q. Guo, Q. Zhao, X. Wang, Z. J. Yong, H. Li, J. P. Ma, Y. Kuroiwa, C. Moriyoshi, L. L. Hu, L. Y. Zhang, L. R. Zheng, H. T. Sun, *Light: Sci. Appl.* **2018**, *7*, 88.

[12] H. F. Shi, Z. F. An, *Nat. Photonics* **2019**, *13*, 74.

[13] T. Aitasalo, P. Dereń, J. Hölsä, H. Jungner, J. C. Krupa, M. Lastusaari, J. Legendziewicz, J. Niittykoski, W. Stręk, *J. Solid State Chem.* **2003**, *171*, 114.

[14] J. Shi, X. Sun, S. Zheng, X. Fu, Y. Yang, J. Wang, H. Zhang, *Adv. Opt. Mater.* **2019**, *7*, 1900526.

[15] H. Lin, G. Bai, T. Yu, M. K. Tsang, Q. Zhang, J. Hao, *Adv. Opt. Mater.* **2017**, *5*, 1700227.

[16] Y. Zhuang, L. Wang, Y. Lv, T.-L. Zhou, R.-J. Xie, *Adv. Funct. Mater.* **2018**, *28*, 1705769.

[17] H. Homayoni, S. Sahi, L. Ma, J. Zhang, J. Mohapatra, P. Liu, A. P. Sotelo, R. T. Macaluso, T. Davis, W. Chen, *J. Lumin.* **2018**, *198*, 132.

[18] B. Qu, B. Zhang, L. Wang, R. Zhou, X. C. Zeng, *Chem. Mater.* **2015**, *27*, 2195.

[19] E. Finley, A. Mansouri Tehrani, J. Brgoch, *J. Phys. Chem. C* **2018**, *122*, 16309.

[20] X. Zheng, B. Zhang, P. De Luna, Y. Liang, R. Comin, O. Voznyy, L. Han, F. P. Garcia de Arquer, M. Liu, C. T. Dinh, T. Regier, J. J. Dynes, S. He, H. L. Xin, H. Peng, D. Prendergast, X. Du, E. H. Sargent, *Nat. Chem.* **2018**, *10*, 149.

[21] C. Collins, M. S. Dyer, M. J. Pitcher, G. F. S. Whitehead, M. Zanella, P. Mandal, J. B. Claridge, G. R. Darling, M. J. Rosseinsky, *Nature* **2017**, *546*, 280.

[22] M. Hayward, M. Green, M. Rosseinsky, J. Sloan, *J. Am. Chem. Soc.* **1999**, *121*, 8843.

[23] C. A. Bridges, G. R. Darling, M. A. Hayward, M. J. Rosseinsky, *J. Am. Chem. Soc.* **2005**, *127*, 5996.

[24] F. Denis Romero, S. J. Burr, J. E. McGrady, D. Gianolio, G. Cibin, M. A. Hayward, *J. Am. Chem. Soc.* **2013**, *135*, 1838.

[25] Y. Tsujimoto, C. Tassel, N. Hayashi, T. Watanabe, H. Kageyama, K. Yoshimura, M. Takano, M. Ceretti, C. Ritter, W. Paulus, *Nature* **2007**, *450*, 1062.

[26] Y. Kobayashi, O. J. Hernandez, T. Sakaguchi, T. Yajima, T. Roisnel, Y. Tsujimoto, M. Morita, Y. Noda, Y. Mogami, A. Kitada, M. Ohkura, S. Hosokawa, Z. Li, K. Hayashi, Y. Kusano, J. Kim, N. Tsuji, A. Fujiwara, Y. Matsushita, K. Yoshimura, K. Takegoshi, M. Inoue, M. Takano, H. Kageyama, *Nat. Mater.* **2012**, *11*, 507.

[27] B. M. Liu, Z. G. Zhang, K. Zhang, Y. Kuroiwa, C. Moriyoshi, H. M. Yu, C. Li, L. R. Zheng, L. N. Li, G. Yang, Y. Zhou, Y. Z. Fang, J. S. Hou, Y. Matsushita, H. T. Sun, *Angew. Chem., Int. Ed.* **2016**, *55*, 4967.

[28] G. Kaur Behrh, H. Serier-Brault, S. Jobic, R. Gautier, *Angew. Chem., Int. Ed.* **2015**, *54*, 11501.

[29] D. Li, K. Lee, B. Y. Wang, M. Osada, S. Crossley, H. R. Lee, Y. Cui, Y. Hikita, H. Y. Hwang, *Nature* **2019**, *572*, 624.

[30] B. V. Fisher, R. E. Morgan, G. O. Phillips, H. W. Wardale, *Radiat. Res.* **1971**, *46*, 229.

[31] S. Subramanian, M. C. R. Symons, H. W. Wardale, *J. Chem. Soc. A* **1970**, *0*, 1239.

[32] Y. Doi, T. Aoba, M. Okazaki, J. Takahashi, Y. Moriwaki, *Calcif. Tissue Int.* **1979**, *28*, 107.

[33] B. S. Chakrabarty, K. V. R. Murthy, T. R. Joshi, *Turk. J. Phys.* **2002**, *26*, 193.

[34] S. Syrotyuk, Y. M. Chornodolskyy, V. Vistovskyy, A. Voloshinovskii, A. Gektin, *Funct. Mater.* **2013**, *20*, 373.

[35] L. Bershov, *Theor. Exp. Chem.* **1973**, *6*, 326.

[36] E. Chaudan, J. Kim, S. Tusseau-Nenez, P. Goldner, O. L. Malta, J. Peretti, T. Gacoin, *J. Am. Chem. Soc.* **2018**, *140*, 9512.

[37] T. Maldiney, A. Lecointre, B. Viana, A. Bessiere, M. Bessodes, D. Gourier, C. Richard, D. Scherman, *J. Am. Chem. Soc.* **2011**, *133*, 11810.

[38] A. M. Srivastava, A. A. Setlur, H. A. Comanzo, W. W. Beers, U. Happek, P. Schmidt, *Opt. Mater.* **2011**, *33*, 292.

[39] P. A. Tanner, C. S. K. Mak, M. D. Faucher, W. M. Kwok, D. L. Phillips, V. Mikhailik, *Phys. Rev. B* **2003**, *67*, 115102.

[40] C. K. Duan, P. A. Tanner, V. Makhov, N. Khaidukov, *J. Phys. Chem. A* **2011**, *115*, 8870.

[41] A. C. Larson, R. B. Von Dreele, *Los Alamos National Laboratory Report LAUR* **2000**, pp. 86–748.

[42] J.-P. Ma, Y.-M. Chen, L.-M. Zhang, S.-Q. Guo, J.-D. Liu, H. Li, B.-J. Ye, Z.-Y. Li, Y. Zhou, B.-B. Zhang, O. M. Bakr, J.-Y. Zhang, H.-T. Sun, *J. Mater. Chem. C* **2019**, *7*, 3037.

[43] H. Wang, D. Yong, S. Chen, S. Jiang, X. Zhang, W. Shao, Q. Zhang, W. Yan, B. Pan, Y. Xie, *J. Am. Chem. Soc.* **2018**, *140*, 1760.

[44] I. D. Ryabov, L. V. Bershov, I. G. Ganeev, *Phys. Chem. Miner.* **1989**, *16*, 374.

[45] H. Nishikawa, *J. Mol. Catal. A: Chem.* **2003**, *206*, 331.

[46] J. P. Perdew, K. Burke, M. Ernzerhof, *Phys. Rev. Lett.* **1996**, *77*, 3865.

[47] G. Kresse, J. Hafner, *Phys. Rev. B* **1993**, *47*, 558.

[48] G. Kresse, J. Furthmüller, *Phys. Rev. B* **1996**, *54*, 11169.

[49] G. Kresse, J. Furthmüller, *Comput. Mater. Sci.* **1996**, *6*, 15.

[50] G. Kresse, D. Joubert, *Phys. Rev. B* **1999**, *59*, 1758.

[51] P. E. Blöchl, *Phys. Rev. B* **1994**, *50*, 17953.

[52] H. J. Monkhorst, J. D. Pack, *Phys. Rev. B* **1976**, *13*, 5188.

[53] M. Neupane, G. Garrett, S. Rudin, J. Andzelm, *J. Phys.: Condens. Matter* **2016**, *28*, 205501.

[54] H.-P. Komsa, T. T. Rantala, A. Pasquarello, *Phys. Rev. B* **2012**, *86*, 045112.

[55] Y. Kumagai, F. Oba, *Phys. Rev. B* **2014**, *89*, 195205.

[56] S. Lany, A. Zunger, *Modell. Simul. Mater. Sci. Eng.* **2009**, *17*, 084002.